Optimal Control Surface Layout for an Aeroservoelastic Wingbox

Bret K. Stanford*

NASA Langley Research Center, Hampton, VA, 23681

This paper demonstrates a technique for locating the optimal control surface layout of an aeroservoelastic Common Research Model wingbox, in the context of maneuver load alleviation and active flutter suppression. The combinatorial actuator layout design is solved using ideas borrowed from topology optimization, where the effectiveness of a given control surface is tied to a layout design variable, which varies from zero (the actuator is removed) to one (the actuator is retained). These layout design variables are optimized concurrently with a large number of structural wingbox sizing variables and control surface actuation variables, in order to minimize the sum of structural weight and actuator weight. Results are presented that demonstrate interdependencies between structural sizing patterns and optimal control surface layouts, for both static and dynamic aeroelastic physics.

I. Introduction

Articulated control surfaces distributed along the trailing edge of a highly-flexible wing structure can be utilized to improve overall flight performance in several ways: cruise drag reduction, maneuver load alleviation, gust rejection, active flutter suppression, etc. Due to the coupled nature of the aeroelastic physics, control surface actuation will have a strong impact on the effective mass, stiffness, and damping of the wing, and design optimization/tailoring studies should reflect this interdependency. As such, several papers have demonstrated optimization of structural wing properties and commanded control surface rotations (quasi-steady and/or dynamic actuation), within a single design loop: see for example Refs. 1 - 4.

Fewer papers exist that optimize (in addition to its commanded actuation) control surface placement and layout, owing to the complexities of this design space. Optimal actuator placement is a well-studied topic for nonaerospace structures (see the review by Padula[5]) and for aeroelastic structures with embedded actuators, such as piezoelectric patches,[6,7] which are easily integrated into a structural wing model. For hinged control surface applications, optimal placement studies are given by Johnson et al.[8] and Weisshaar and Nam[9] using gradient-based optimization, and Viswamurthy and Ganguli[10] and Kolonay and Kobayashi[11] using nongradient-based optimization. The former design technique is generally preferred to the latter, due to its ability to handle large numbers of design variables, but will also struggle with local minima.

Rather than explicitly utilize control surface location design variables, as done in the literature cited above, the current work poses the problem as a combinatorial one: a bank of control surfaces are distributed along the trailing edge of a wingbox, and the optimizer must decide which to retain and which to discard. These problems are commonly solved[5] using nongradient-based optimizers, but this is not an option here, as a very large number of structural wingbox design variables are to be handled simultaneously with the control surface variables. Alternatively, a topology design variable may be attached to each control surface actuator, ranging from zero (the control surface actuator is entirely removed, leaving behind only a rigid outer mold line) to one (the control surface is fully utilized). A combination of implicit and explicit penalties on intermediate values may be used during the optimization process to push each topology variable to its extreme (zero or one) as the process converges.

In the current work, structural sizing design variables, control surface actuation/scheduling design variables, and control surface layout/topology design variables, are all optimized simultaneously for the Common Research Model (CRM), a generic transport configuration. This is done within the context of maneuver load

*Research Aerospace Engineer, Aeroelasticity Branch, bret.k.stanford@nasa.gov, AIAA Senior Member.

alleviation (MLA) and active flutter suppression (AFS). Different classes of design variables are phased into the optimization results incrementally, in order to track changes in wing performance metrics and their underlying aeroelastic physics, as the design space is expanded.

II. Control Surface Actuation and Topology Design Variables

The ideas used here for control surface layout design are taken from the topology optimization literature, namely the SIMP method (Solid Isotropic Material with Penalization).[12] The method is predicated on a nonlinear power law relationship between the topological design variable of an element and its elastic modulus, which makes the ratio of stiffness-to-mass less attractive for intermediate topologies (i.e., between zero and one). A similar concept is found to be useful here, where the rotation of a given control surface is computed as:

$$\theta_i = \overline{\theta_i} \cdot (x_i)^p \tag{1}$$

where $\overline{\theta_i}$ is the rotation of the i^{th} control surface as decided upon by the optimizer, x_i is the topological design variable, p is an integer, and θ_i is the control surface rotation actually passed to the aeroelastic solver. The mass of the i^{th} actuator is computed as:

$$m_i = m_{0,i} \cdot x_i \tag{2}$$

where $m_{0,i}$ is the set actuator mass, and m_i is the mass actually utilized for aeroelastic analysis.

If a given x_i is set (by the optimizer) to zero, clearly the optimizer's choice for the i^{th} control surface actuation becomes immaterial, as the actuator has been removed and the control surface rigidized. If x_i is set to one, the desired control surface actuation is passed to the aeroelastic solver as-is. Intermediate values (e.g., $x_i = 0.5$) may in general be attractive to the optimizer, as they present a compromise between reducing total weight (Eq. 2) and still allowing for some contribution to maneuver load alleviation (for example) from the i^{th} control surface. Values of p greater than one in Eq. 1 diminish this compromise, just as in the SIMP method, pushing most x_i variables to the desired extremes of zero or one during the optimization process.

III. Transport Configuration Test Case

All of the work in this paper is conducted on a conceptual high aspect ratio Common Research Model (CRM). The $1g$ outer mold line for a lower aspect ratio (AR = 9) CRM is described in Ref. 13, and a jig shape CRM wingbox subsequently developed by Kenway et al.[14] A span extension of this model increased the aspect ratio from 9 to 13.5; the latter configuration (shown in Fig. 1) is used here. This transonic transport has a wing span of 72 m, a mean aerodynamic chord of 6.3 m, a taper ratio of 0.25, a sweep angle of 35°, and a cruise Mach number of 0.85. The topology of the wingbox in Fig. 1 consists of 58 ribs, leading and trailing spars, and upper and lower surface skins. All shell members are outfitted with T-shaped stiffeners, where the flange is bonded to the shell members. The stiffeners are not modeled explicitly, but instead smeared into the shell stiffness properties.[15]

An aluminum finite element model of this wingbox is composed of 21,300 triangular finite elements. Non-modeled secondary weight (of fasteners, etc.) is captured by increasing the structural density by a factor of 1.25. Nodes along the wing centerline are given a symmetric boundary condition; nodes along the wing root are given a pinned boundary condition.

Finally, twenty articulated control surfaces are distributed along the trailing edge of the wing from root to tip, also seen in Fig. 1. The mass of each actuator used to drive each control surface, $m_{0,i}$, is set based on an initial estimate of the hinge moments encountered during maneuver loading, using a constant mass-per-hinge-moment value. This actuator mass value ranges from 214.5 kg (root) to 26.3 kg (tip). The mass of each control surface flap is proportional to the surface area of the wedge, and ranges from 140.4 kg (root) to 35.4 kg (tip). A hinge spring attached to each control surface is connected back to the trailing spar via interpolation elements. For static aeroelastic simulations, the hinge spring is sized such that, when the worst-case hinge moment is applied, the control surface rotates no more than 0.1 rad. For dynamic aeroelasticity, a different hinge spring stiffness is used: each spring is sized such that the isolated natural frequency of each control surface is 35 Hz. Both choices are made to effectively remove any passive rotations of each control surface, but not rigidize to such a degree that numerical difficulties may arise. Inertial properties of each

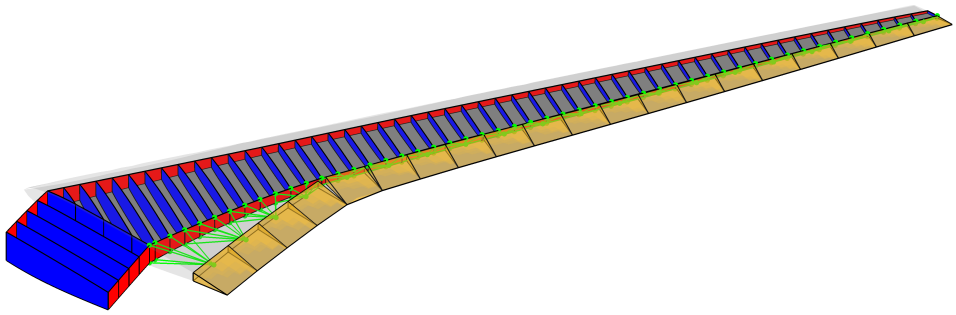

Figure 1. Wingbox, outer mold line, and control surfaces of the high aspect ratio CRM.

control surface, and stiffness properties of each hinge spring, are integrated into the shell-based finite element model of the wingbox, by considering each control surface rotation as an additional degree of freedom.

The paneling scheme used to model steady and unsteady linear aerodynamic loads over the vehicle is shown in Fig. 2, with a total of 4,150 panels. A finer mesh is used toward the hinge line of the control surfaces, in order to improve the accuracy of the aeroservoelastic loads generated by deflections. Non-structural lumped mass distributions are also shown in the figure, to model the fuel (44,800 kg), engine (11,400 kg), and various unmodeled components in the leading and trailing edges of the wing (5,480 kg). The total mass of the 20 control surfaces and their actuators is 3,935 kg, and a fixed mass of 63,700 kg is used to model the remainder of the half-airplane (fuselage, etc.). Typical structural masses (for a single wingbox) will range during optimization from 15,000 to 20,000 kg. The TOGW for the entire vehicle is then roughly 300,000 kg.

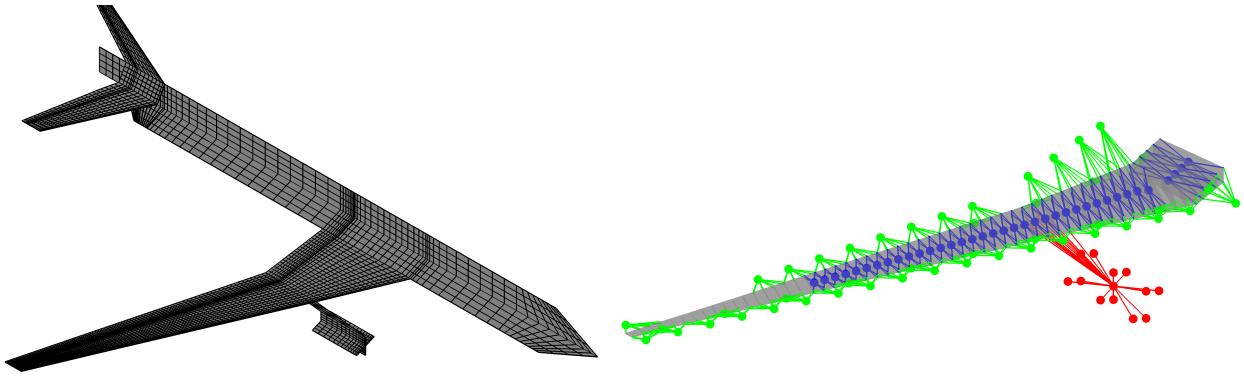

Figure 2. Aerodynamic paneling (left) and non-structural lumped mass distribution (right).

IV. Maneuver Load Alleviation

Airplane maneuvers are considered to occur slow enough to warrant only static aeroelastic modeling: dynamic aeroelastic effects are ignored in this section. Maneuver loads are computed with the following equation:

$$\begin{bmatrix} \boldsymbol{K} & -q\cdot\boldsymbol{Q} & \boldsymbol{0} & \boldsymbol{0} \\ -\boldsymbol{P} & \boldsymbol{D} & -\boldsymbol{L}_\alpha & -\boldsymbol{L}_\delta \\ \boldsymbol{0} & q\cdot\boldsymbol{S}_L^T & 0 & 0 \\ \boldsymbol{0} & q\cdot\boldsymbol{S}_m^T & 0 & 0 \end{bmatrix} \cdot \begin{Bmatrix} \boldsymbol{x} \\ \boldsymbol{C}_p \\ \alpha \\ \delta \end{Bmatrix} = \begin{Bmatrix} N\cdot\boldsymbol{F}_{grav}+\boldsymbol{F}_{thrust} \\ \boldsymbol{L}_{jig} \\ N\cdot W \\ 0 \end{Bmatrix} + \begin{Bmatrix} \boldsymbol{Q}_{HM} \\ \boldsymbol{0} \\ 0 \\ 0 \end{Bmatrix} \cdot \boldsymbol{\theta} \tag{3}$$

The first row of Eq. 3 is the finite element analysis: $\boldsymbol{K}$ is the stiffness matrix, and $\boldsymbol{x}$ is the solution vector, which includes both structural wingbox deformations and control surface rotations. Forcing functions include self-weight inertial loading, $\boldsymbol{F}_{grav}$ (scaled by the load factor N), thrust loading, $\boldsymbol{F}_{thrust}$, from the engine,

and aerodynamic forces. Aerodynamic forces are written as $q \cdot \boldsymbol{Q} \cdot \boldsymbol{C}_p$, where $\boldsymbol{C}_p$ is a vector of differential pressure coefficients acting on each panel, $\boldsymbol{Q}$ is an interpolation function derived from a finite plate spline (FPS),[16] and q is the dynamic pressure. Commanded quasi steady actuation inputs, θ_i (from Eq. 1), are collected in the vector $\boldsymbol{\theta}$. These are applied to the finite element model as hinge moments applied to each control surface hinge spring, via the matrix $\boldsymbol{Q}_{HM}$.

The second row of Eq. 3 is the aerodynamic analysis, where $\boldsymbol{D}$ is the matrix of aerodynamic influence coefficients (AIC). This equation is driven by downwash due to angle of attack, $\boldsymbol{L}_\alpha \cdot \alpha$ (where $\boldsymbol{L}_\alpha$ is a linear operator that converts the scalar angle of attack into a downwash at each panel), elevator deflection, $\boldsymbol{L}_\delta \cdot \delta$, built-in camber/twist of the wing and tail jig shapes, $\boldsymbol{L}_{jig}$, and downwash induced by structural wing deformation. This latter term is written as $\boldsymbol{P} \cdot \boldsymbol{x}$, where $\boldsymbol{P}$ is a second interpolation function, also derived from FPS-based methods.

Trim equations are written in the 3rd and 4th rows of Eq. 3: $q \cdot \boldsymbol{S}_L$ and $q \cdot \boldsymbol{S}_m$ convert the differential pressure vector, $\boldsymbol{C}_p$, into a total aerodynamic lift and aerodynamic pitching moment (about the aircraft center of gravity). Lift must offset the total weight of the vehicle ($N \cdot W$), and the pitching moment must be zero.

The second type of load case considered here is an inertial-only load case, with neither aeroelasticity, trimming mechanisms, nor control surface actuation involved. This is meant to emulate landing loads or taxi bump loads, with wing deformation simply computed by:

$$\boldsymbol{K} \cdot \boldsymbol{x} = N \cdot \boldsymbol{F}_{grav} \tag{4}$$

Having solved for the wing deformation in Eqs. 3 or 4, von Mises stresses are computed for each finite element, including a knock-up (safety) factor. The wingbox in Fig. 1 is broken into patches (one patch per rib, per rib-delineated skin panel, and per rib-delineated spar section, for 283 total patches), and the Kreisselmeier-Steinhauser (KS) function[17] is used to compress all of the elemental failure function values within a given patch into a single metric. Next, buckling analyses are run for each stiffened panel in the upper and lower skins, using a Rayleigh-Ritz method (assumed buckling modes). Both global buckling of a stiffened panel (bordered by ribs and spars) and local buckling between each stiffener is computed, where simply-supported boundary conditions are used for both scenarios. As with the stress metrics, each buckling eigenvalue for a given stiffened panel is compressed into a single KS function.

Five load cases are utilized here, summarized in Table 1. Load cases 1 and 2 are both run at $2.5g$, but case 1 features maneuver load alleviation from the control surfaces (θ_i in Eq. 1), whereas case 2 does not: θ_i is set to 0. Forcing the optimizer to account for load cases that do not benefit from control surface-based aeroelastic tailoring (albeit at a lower safety factor) prevents overly-large mass reductions and injects a level of risk-reduction into the design process. A similar open/closed-loop dynamic is used for load cases 3 and 4, at $-1g$. The final load case 5 is a simple $2g$ inertial-only landing load, and is not aeroelastically coupled. Aeroelastic load cases 1-4 are computed with Eq. 3, inertial case 5 is computed with Eq. 4.

Table 1. Summary of static aeroelastic load cases.

Case	N	Mach	Altitude	Safety Factor	Actuator Status
1	2.5	0.64	0 ft	1.5	closed-loop
2	2.5	0.64	0 ft	1.3	open-loop
3	-1	0.64	0 ft	1.5	closed-loop
4	-1	0.64	0 ft	1.3	open-loop
5	2	-	-	1.5	open-loop

A. MLA Optimization Definition

The gradient based optimization problem solved here is given in Table 2. The objective function, M, is the sum of the structural wingbox weight and the control surface actuator weight (m_i). Design variables $\boldsymbol{q}$ include the thickness of each patch shell (ranging from 3 to 30 mm), the thickness of the stiffeners attached to each patch (3 to 30 mm), and the height of the stiffeners (30 to 100 mm). Additional design variables

include the commanded rotation for each control surface ($\overline{\theta_i}$) for each closed-loop load case (ranging from $-10°$ to $10°$), as well as the topological/layout variables x_i (ranging from 0 to 1).

Table 2. MLA optimization definition.

minimize:	$M(\boldsymbol{q})$	
subject to:	$\boldsymbol{q}_{LB} \leq \boldsymbol{q} \leq \boldsymbol{q}_{UB}$	
	$KS_{\sigma,i} \leq 1$	$i = 1, ..., N_\sigma \cdot N_L$
	$KS_{\mu,i} \leq 1$	$i = 1, ..., N_\mu \cdot N_L$
	$KS_{t/t_s} \leq 1$	
	$KS_{AR} \leq 1$	
	$\sum(x_i - x_i^2) \leq \delta_x$	

N_L is the number of static load cases in Table 1, KS_σ are the stress aggregation parameters (N_σ per load case), and KS_μ are the buckling aggregation parameters (N_μ per load case). It is desired that, for a given design patch, the shell thickness be within 2.5 mm of the stiffener thickness. These constraints are normalized to 1 for each design patch, and then all aggregated into a single metric, KS_{t/t_s}. Similarly, the aspect ratio of each stiffener should not be greater than 15, which is compressed into a single constraint, KS_{AR}. The final constraint in Table 2 controls intermediate x_i values. For all cases in this paper, the implicit penalty of the SIMP method is able to mostly push each x_i to 0 or 1, and so δ_x is set to a large value for the bulk of the optimization. Once the optimizer has converged, δ_x is dropped to 0, which explicitly forces each x_i to 0 or 1.

Each set of design variables is passed through a linearly-decaying cone-shape filter[12] in order to prevent the difference in stiffness between adjacent patches, or the difference in actuation between adjacent control surfaces, from being too large. A linear matrix relationship can be built between the unfiltered design variables (which are directly created by the optimizer), and the filtered design variables (which are used to construct the aeroelastic model). All gradient-based optimization problems are solved with the Globally-Convergent Method of Moving Asymptotes tool (GCMMA).[18] Design derivatives are analytically computed via the adjoint method.[19]

B. MLA Optimization Results

Aeroelastic optimization results are shown here in 4 stages, summarized in the convergence plot of Fig. 3. The first stage considers only structural design variables (shell thickness, stiffener thickness, and stiffener height of each patch), with each control surface rotation variable $\overline{\theta_i}$ held fixed at $0°$ and each control surface layout variable x_i fixed at 1. With active maneuver load alleviation turned off, load cases 1 and 2 (and 3 and 4) become identical, and the cases with the lower safety factor (2 and 4) have no impact on the design problem. Convergence for this stage of the design process occurs in Fig. 3 between iterations 1 and 30, starting with an unsized structure, and ending when the difference in objective function between consecutive iterations is less than 10^{-5}. The mass of the optimal structure, shown in Fig. 4, is 19,189 kg. The actuator mass (2,262 kg) is constant during the first design phase, as this portion of the system is held fixed.

The second phase of the design process (between iterations 30 and 58 in Fig. 3) adds the control surface rotation design variables $\overline{\theta_i}$ to the optimization problem, though each layout variable x_i is still fixed at 1 (i.e., the optimizer is forced to use the full set of 20 control surfaces). Commanded rotations are bounded by $\pm 10°$, and are individually optimized for each control surface, and for each closed-loop load case (1 and 3). This leaves 40 additional $\overline{\theta_i}$ design variables. The closed-loop load cases have higher safety factors (1.5), but also benefit from control surface-based load alleviation. Conversely, the open-loop load cases have a lower safety factor (1.3), but do not benefit from aeroelastic control: as such, the constraints attached to both sets of load cases (stresses and buckling) will contribute to the design process.

The addition of control surface rotation design variables affords substantial structural mass reductions, down from 19,189 kg to 13,862 kg, a 27.7% reduction. As before, actuator mass is constant for this portion of the design process. For a positive load case, the basic trade-off exploited by the optimizer is to use the control surfaces to alleviate outboard loads (decreased bending moment), which then allows for a reduction in structural mass without violating stress or buckling constraints. The decreased outboard lift is offset by

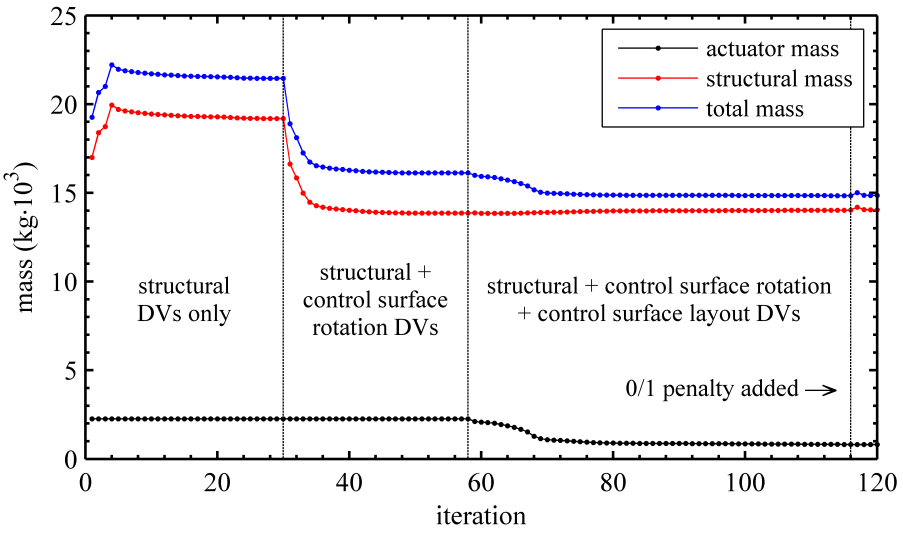

Figure 3. Convergence history of the MLA aeroelastic optimization process.

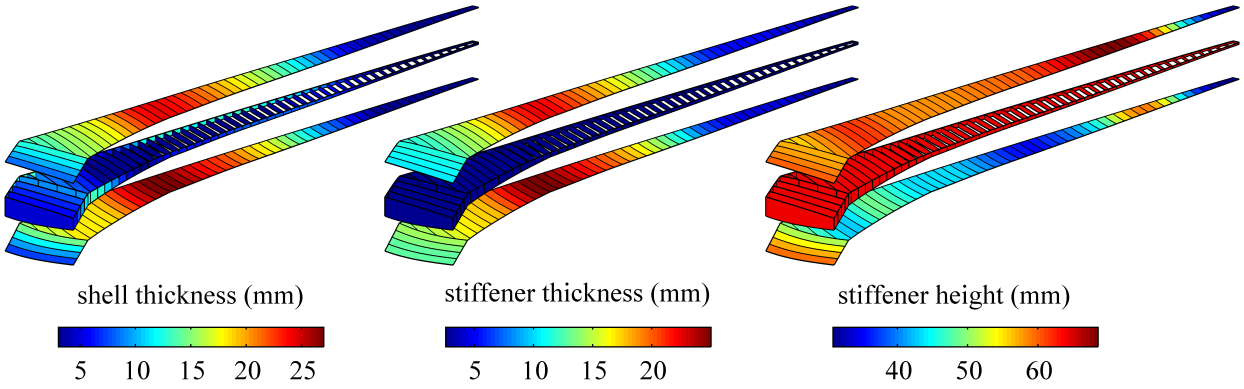

Figure 4. Optimal wingbox structure without control surface manuever load alleviation.

positive lift generation from the inboard control surfaces, in order to maintain trim without a large increase in angle of attack. Optimal control surface rotations for both load cases are shown in Fig. 5.

The third phase of the design process (between iterations 58 and 116 in Fig. 3) adds the x_i variables, which allows the optimizer to simultaneously alter the wingbox structural details, the control surface layout, and the commanded rotations of those control surfaces selected for use. Actuator mass drops during this phase, from 2,262 kg to 819 kg. As a decrease in actuator mass also decreases the actuator efficacy (Eqs. 1 and 2), the maneuver load alleviation into the wingbox becomes less prominent, and structural mass increases during this design phase, from 13,862 kg to 14,029 kg. The sum of actuator and structural mass, the objective function for this problem, does decrease during this design phase, however.

Despite the implicit SIMP-based penalty on intermediate x_i variables, the optimizer is unable to push every layout variable exactly to the extremes of 0 or 1, creating an unrealistic situation where some actuator/control surface pairs "partially" exist. The fourth and final phase of the design process in Fig. 3 enforces the final constraint in Table 2, by dropping δ_x to 0. Meeting this constraint forces the optimizer to pay a small penalty in terms of structural mass (from 14,029 kg to 14,043 kg), though actuator mass decreases from 819 kg to 812 kg. The optimal control surface layout, and the commanded rotations of those control surfaces, is shown in Fig. 5, for comparison with the previous result. Given these small shifts in mass values, it can be inferred that the SIMP method can nearly achieve a 0/1 solution on its own.

The optimizer chooses to retain the furthest 2 inboard control surfaces, two located near midspan, and three closer to the wingtip. The remaining 13 control surfaces have been rigidized, and their actuator masses removed. The retention of the inboard actuator is a testament to its role during the aeroelastic optimization

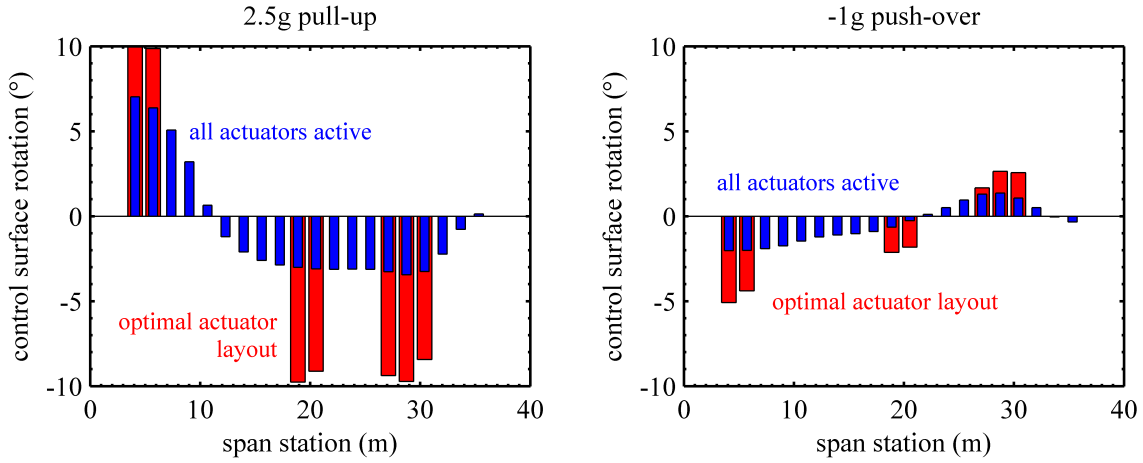

Figure 5. Optimal control surface rotation design variables during MLA.

process: it is the heaviest actuator (214 kg, versus 26 kg for the outboard actuator), and the optimizer would otherwise have every incentive to remove it. Control surface rotations for each retained actuator are the same sign as those seen for the case when the entire bank of control surfaces is active, though much larger in magnitude. This increase is presumably due to the need for each actuator to provide a greater aerodynamic force, since there are fewer of them.

The aeroelastic lift and twist distribution for several designs are shown in Fig. 6: the wing designed with only structural variables, designed with both structural variables and a full bank of control surfaces, the wing with the optimal actuator layout, and a rigid wing. Discontinuities are shown in these lift plots at the wing root (2.6 m) and the engine mount location (11.1 m). The large passive deformations of this swept wing (without control surface maneuver load alleviation) shows substantial outboard lift and twist reductions relative to the rigid wing, prompting an increase in angle of attack to maintain trim (vehicle angle of attack is evidenced by the wing root angle in Fig. 6).

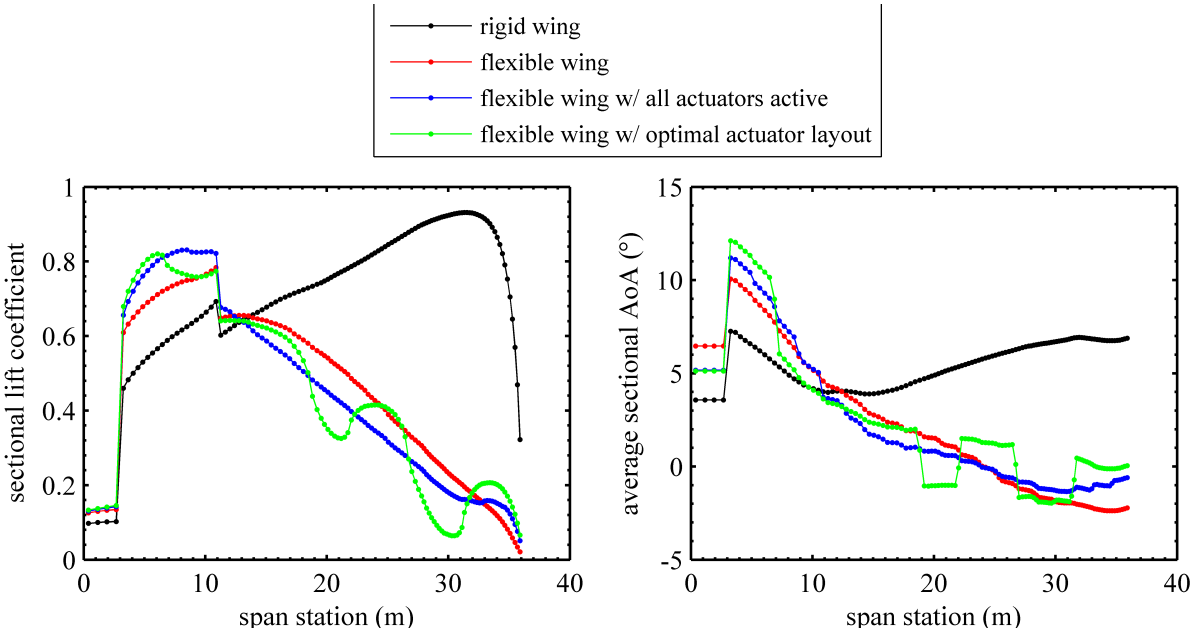

Figure 6. Sectional lift coefficient (left) and angle of attack (right) for the three optimal designs, as well as a rigid wing, during the 2.5g maneuver.

The aeroelastic design with the full bank of active actuators in Fig. 6 is able to further decrease the

bending moment through an explicit lift reduction of the outboard control surfaces (negative rotations), as well as positive rotations at the root. These latter motions can help maintain trim (last two rows of Eq. 3) without increasing the bending moment. The final design in Fig. 6 with the optimal layout of control surfaces is driven by these same mechanisms, with spanwise undulations in lift resulting from the discontinuous control surface-based downwash.

Given their large moment arm, it is perhaps surprising that the optimizer does not make use of the control surfaces at the wingtip. When the optimizer uses all 20 control surfaces, rotations at the tip are very small; when layout design variables are included, the optimizer removes the 3 outer actuators entirely. This is due to the torsional flexibility of the high aspect ratio CRM model used here, leading to decreased effectiveness of the actuators at the wingtip. A positive control surface rotation (trailing edge down) nominally produces positive lift, but this force is diluted by the nose-down wing twisting. Fig. 7 computes the % change in root bending moment due to a unit rotation of each control surface. For the flexible data in this figure, the outboard control surfaces are "reversed", in the sense that the change in bending moment is opposite the expected trend. Control surfaces near the wing root (i.e., with the smallest moment arm) actually have the largest impact on bending moment in Fig. 7, which is due to flexible trimming requirements: inboard lift generation allows the optimizer to reduce the angle of attack. The rigid wing data in Fig. 7 shows a more expected trend, with larger bending moment impacts from outboard control surfaces.

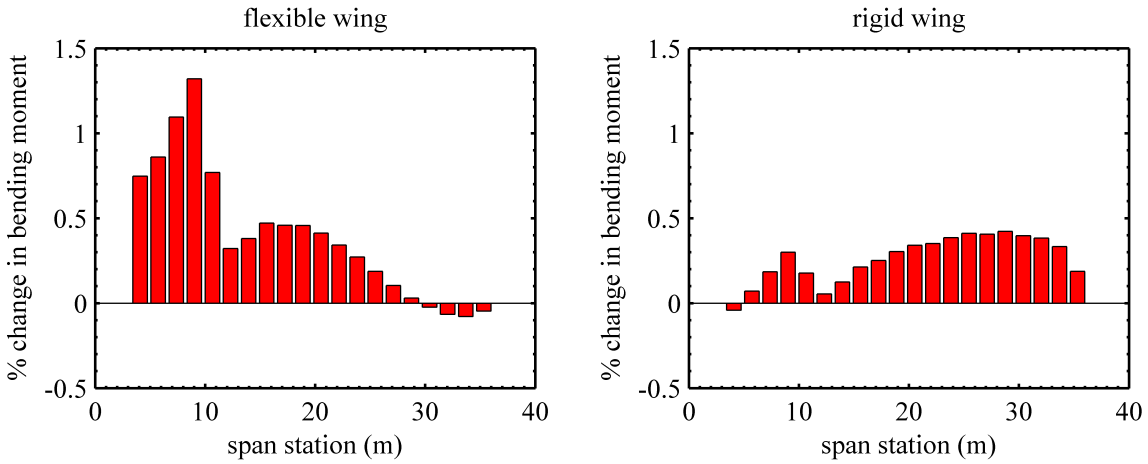

Figure 7. % change in 2.5g root bending moment due to a 1° control surface rotation: flexible wing (left) and rigid wing (right).

The optimizer could passively stiffen the wing in such a way to improve the effectiveness of these outboard control surfaces, but this would evidently result in a heavier system than the solution shown in Fig. 4 and Fig. 5, where the optimizer simply ignores (and removes) these outboard surfaces in favor of actuators with a smaller moment arm. The moment arm of a control surface is less of a predictor for MLA-effectiveness in any case, given the complex aeroelastic trim mechanisms seen in Fig. 7.

C. Dependence of MLA Optimization on the Number of Actuators

As noted above, as the optimizer decreases the number of actuators it must increase the structural weight, as the reduced levels of MLA require the wingbox to be passively stiffened in order to satisfy stress and buckling constraints. In Fig. 3, this mass penalty is mild, rising from 13,862 to 14,043 kg, a 1.3% increase (actuator mass, by contrast, decreases by 64.1 %). This essentially means that MLA with 20 control surfaces is only mildly better than MLA with 7 control surfaces. To further understand this trade-off, an additional constraint is added to Table 2, which stipulates that the number of control surfaces be less than some threshold. The shift in the optimal mass details and the optimal control surface layout, as a function of this threshold, is shown in Fig. 8. This figure does not consider more than 7 control surfaces, since this is the number naturally selected by the optimizer in Fig. 3.

It can be seen that decreasing the required number of actuators from 7 to 3 leaves the objective function (the sum of actuator and wingbox structural mass) largely unchanged, with a very small penalty. Actuator mass decreases when moving from 7 to 3, of course, but is nearly offset by the growing structural mass

penalty. Three control surfaces is the fewest number with which the optimizer can still practice the basic mechanism outlined above: outboard load alleviation (from a single control surface at midspan), offset by positive load generation at the root to maintain trim. Once the optimizer is forced to use 2 or fewer control surfaces, this mechanism is destroyed: penalties in both structural mass and summed structural-actuator mass are substantial. For the limiting case of zero actuators, the structural wingbox mass rises to 19,835 kg. This value is higher than the structural mass seen in the first phase of Fig. 3 (19,189 kg), where all of the actuators are present, but control surface rotations are frozen. The latter case clearly benefits from the inertial relief of the fully-populated actuator masses, even if those actuators are not being used for MLA.

When forced to choose only a few control surfaces, the optimizer retains those closest to the root in Fig. 8. This is an unexpected result, but follows from the trends seen in Fig. 7: the bending moment reductions (and by proxy, overall MLA effectiveness) obtained from inboard lift enhancement (which allows for a reduction in overall angle of attack), are superior to using outboard load alleviation. This is likely to be a configuration-dependent result, in the sense that a lower aspect ratio wing, with lower bending and torsional flexibility, would likely find outboard control surfaces more effective and more attractive during layout optimization.

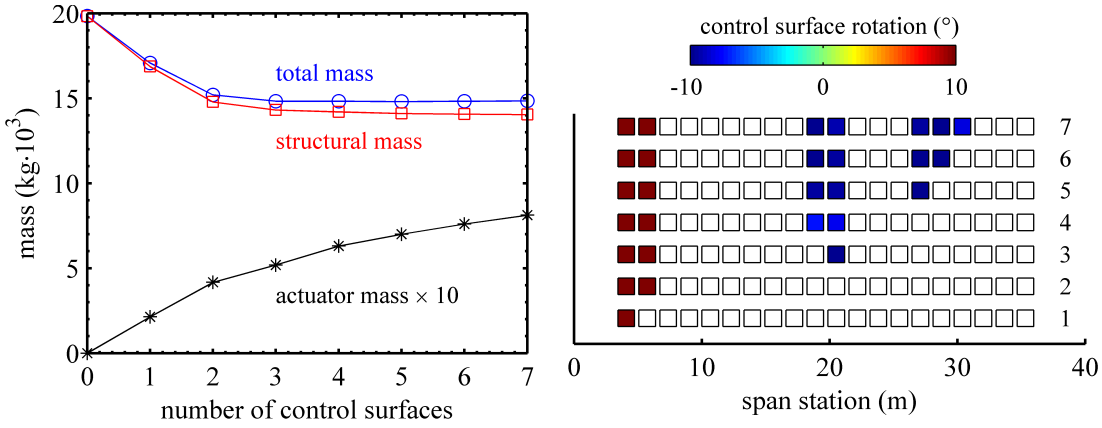

Figure 8. Shift in optimal mass properties (left) and optimal control surface layout (right), with changes in the required number of control surfaces.

V. Active Flutter Suppression

Exercises to this point have included only static aeroelastic physics, with control surfaces used for MLA. In this section, dynamic aeroelastic metrics are included as constraints in the form of flutter margins, with control surfaces used for AFS. In order to isolate and understand the effects of AFS, control surface-based MLA is not considered in this section. In reality, the optimal control surface layout will be a compromise across a wide range of static and dynamic load cases, with oscillatory actuation utilized during AFS superimposed upon the quasi-steady actuation utilized during MLA.[2] These issues are ignored for the preliminary case studied here.

The dynamic aeroelastic behavior of the wing is modeled in the time domain, via modal coordinates.[20] Mode shapes of the flexible wing are combined and orthogonalized with control surface modes (one Ritz vector per control surface),[21] and the combined vector of modal amplitudes is computed as:

$$\begin{Bmatrix} \dot{\boldsymbol{x}}_m \\ \ddot{\boldsymbol{x}}_m \\ \dot{\boldsymbol{x}}_A \end{Bmatrix} = \begin{bmatrix} \boldsymbol{I} & \boldsymbol{0} & \boldsymbol{0} \\ \boldsymbol{0} & \overline{\boldsymbol{M}} - \frac{q \cdot b^2}{U^2} \cdot \boldsymbol{A}_2 & \boldsymbol{0} \\ \boldsymbol{0} & \boldsymbol{0} & \frac{b}{U} \cdot \boldsymbol{I} \end{bmatrix}^{-1} \cdot \begin{bmatrix} \boldsymbol{0} & \boldsymbol{I} & \boldsymbol{0} & \cdots & \boldsymbol{0} \\ -\overline{\boldsymbol{K}} + q \cdot \boldsymbol{A}_0 & -\overline{\boldsymbol{C}} + q \cdot \boldsymbol{A}_1 & q \cdot \boldsymbol{A}_2 & \cdots & q \cdot \boldsymbol{A}_{n+2} \\ \boldsymbol{0} & \frac{b}{U} \cdot \boldsymbol{I} & -\gamma_1 \cdot \boldsymbol{I} & \cdots & \boldsymbol{0} \\ \vdots & \vdots & \vdots & \ddots & \vdots \\ \boldsymbol{0} & \frac{b}{U} \cdot \boldsymbol{I} & \boldsymbol{0} & \cdots & -\gamma_n \cdot \boldsymbol{I} \end{bmatrix} \cdot \begin{Bmatrix} \boldsymbol{x}_m \\ \dot{\boldsymbol{x}}_m \\ \boldsymbol{x}_A \end{Bmatrix} \tag{5}$$

where b is the half-mean chord, and $\overline{\boldsymbol{M}}$, $\overline{\boldsymbol{K}}$, and $\overline{\boldsymbol{C}}$ are the reduced mass, stiffness, and damping matrices.

$\boldsymbol{A}_i$ are the generalized aerodynamic functions resulting from the rational function approximation, and γ_i are the corresponding lag roots (n total). $\boldsymbol{x}_m$ is the vector of modal amplitudes (wing deformation and control surface rotation), and $\boldsymbol{x}_A$ is the vector of aerodynamic states.

Eq. 5 computes open-loop dynamics. Closed-loop dynamics may be computed by augmenting Eq. 5 with a control input:

$$\dot{\boldsymbol{x}}_{ASE} = \boldsymbol{A} \cdot \boldsymbol{x}_{ASE} + \boldsymbol{B} \cdot \boldsymbol{u}_{ASE} \tag{6}$$

where $\boldsymbol{x}_{ASE}$ is the state vector from Eq. 5 and $\boldsymbol{A}$ is the matrix from Eq. 5. $\boldsymbol{u}_{ASE}$ is a vector of input control surface rotations (one per control surface), analogous to the quasi-steady θ_i variables. $\boldsymbol{B}$ is a matrix that converts those commanded rotations into generalized modal forces. Similar to the quasi-steady Eq. 1, the dynamic effectiveness of each control surface must be tied to its layout variable x_i:

$$\boldsymbol{B} = \overline{\boldsymbol{B}} \cdot \begin{bmatrix} (x_1)^p & & & \\ & (x_2)^p & & \\ & & \ddots & \\ & & & (x_I)^p \end{bmatrix} \tag{7}$$

where $\overline{\boldsymbol{B}}$ is the baseline conversion matrix computed with each x_i set to one. As before, values of p greater than one will implicitly push each x_i to the extremes of zero or one[12] during the AFS optimization process.

The controller used here is a simple Linear Quadratic Regulator (LQR), with full-state feedback assumed of the form:

$$\boldsymbol{u}_{ASE} = -\boldsymbol{K}_{LQR} \cdot \boldsymbol{x}_{ASE} \tag{8}$$

The feedback matrix is found which minimizes the performance index:[22]

$$J = \frac{1}{2} \cdot \int_0^\infty (\boldsymbol{x}_{ASE}^T \cdot \boldsymbol{Q} \cdot \boldsymbol{x}_{ASE} + \boldsymbol{u}_{ASE}^T \cdot \boldsymbol{R} \cdot \boldsymbol{u}_{ASE}) \cdot dt \tag{9}$$

where $\boldsymbol{Q}$ is the state weighting matrix, and $\boldsymbol{R}$ is the control weighting matrix. For this work, $\boldsymbol{Q}$ is computed from a unit-weighting of the displacement of eight finite element nodes uniformly distributed throughout the wing: two chordwise and four spanwise. $\boldsymbol{R}$ is set as a diagonal matrix, with each member fixed at 250.

Eigenvalues of either the open-loop Eq. 5 or the closed-loop Eq. 6 are given by $s = g + i \cdot \omega$. For a given Mach number, these eigenvalues may be tracked across a range of matched point equivalent air speeds. Speeds at which a given eigenvalue crosses into the right-half plane ($g = 0$) are flutter points.

A. AFS Optimization Definition

The optimization details in this section closely resemble those in Table 2. The objective function is again the sum of the structural wingbox weight and the control surface actuator weight (m_i). Static aeroelastic stress (KS_σ) and buckling (KS_μ) constraints are attached to load cases 2, 4, and 5 in Table 1; closed-loop MLA cases 1 and 3 are ignored here, as previously noted. The KS_{t/t_s}, KS_{AR}, and δ_x constraints are all enforced as before. Three additional constraints are imposed: an open-loop flutter constraint, a closed-loop flutter constraint, and control cost constraint stipulating that J from Eq. 9 must be less than some threshold.

A flutter constraint is formulated by imposing upper limits on the damping g of each mode, at all equivalent air speeds (U_{EAS}) of interest.[23] Specifically, each damping value is constrained to lie beneath the piecewise polynomial:

$$g \leq \begin{cases} 0 & 0 \leq U_{EAS} \leq U^* \\ c \cdot (U_{EAS} - U^*)^2 & U_{EAS} > U^* \end{cases} \tag{10}$$

The minimum allowable flutter equivalent air speed is U^*, computed from the desired flutter margin and the flight envelope (using a 185 m/s dive speed). The quadratic scaling parameter c is set to 500.

Critical U_{EAS} points (local minima) of the inequality in Eq. 10 are computed and lumped together into a single KS constraint. As above, if this constraint is greater than one, then Eq. 10 is not satisfied, and the structure does not meet the required flutter margin. A separate KS constraint is utilized for each

considered Mach number, for both open- and closed-loop dynamics. Analytical flutter derivatives are simply computed with eigenvalue differentiation techniques[19] via a fixed-mode approximation. For the case of a closed-loop constraint, derivatives of the feedback matrix $\boldsymbol{K}_{LQR}$ and the performance index J are computed using methods in Ref. 24.

Design variables $\boldsymbol{q}$ include patchwise shell thickness, stiffener thickness, and stiffener height, as well as the topological/layout variables x_i. Quasi-steady control surface rotations, $\overline{\theta_i}$, are not included here, as MLA is not considered in this section. A final design variable is U_{LQR},[1] the flight condition at which the feedback matrix $\boldsymbol{K}_{LQR}$ is computed in Eq. 9. In addition to being able to remove control surfaces via x_i, U_{LQR} gives the optimizer a strong influence over the behavior of the controller. Large values of the U_{LQR} control design point (relative to the open-loop flutter point) will stabilize the system at U_{LQR}, as guaranteed by the LQR methodology,[22] but the control cost, J, will be high. Small values of U_{LQR} may not provide a closed-loop flutter point measurably better than the open-loop point, but the control cost will be low.

B. AFS Optimization Results

Convergence of the AFS optimization process is shown in stages in Fig. 9. The first stage considers only static aeroelastic optimization (no flutter), with structural design variables only. The baseline design for this case is the converged design from stage 1 of Fig. 3. The only difference between these two design formulations is the removal of MLA load cases 1 and 3: this allows the optimizer to feasibly remove a large amount of structural material, with the structural mass dropping from 19,189 kg to 13,870 kg. Although optimized without flutter metrics, the open-loop eigenvalue migration behavior of this wing is shown in Fig. 10. Structural modes ($\boldsymbol{x}_m$ from Eq. 5), aerodynamic lag roots ($\boldsymbol{x}_A$), and control surface modes are all noted in the figure, with control surface frequencies emanating from the specified wind-off value of 35 Hz (as discussed above, each control surface hinge spring is tuned to obtain this frequency).

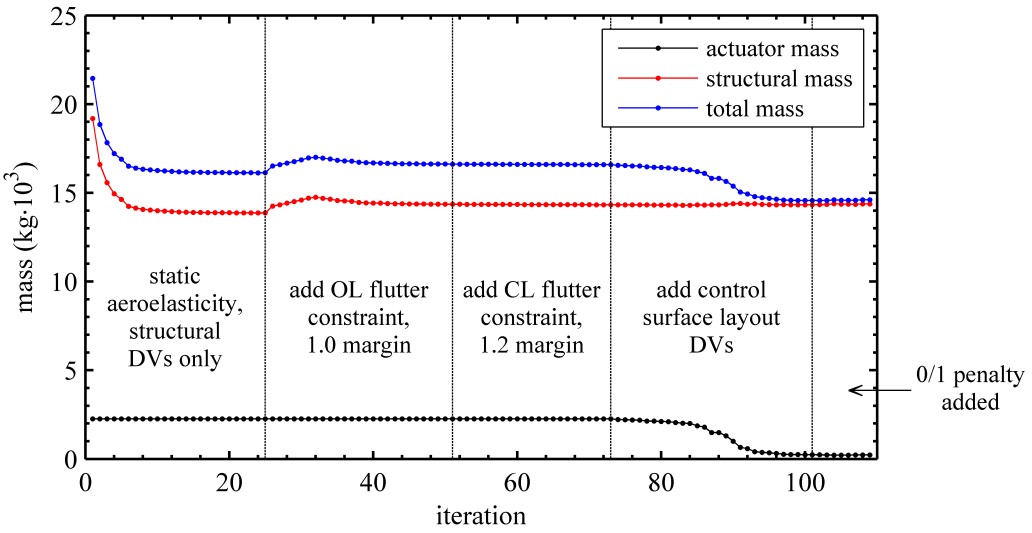

Figure 9. Convergence history of the AFS aeroelastic optimization process.

Three flutter mechanisms can be seen in Fig. 10. The second structural mode (a second bending mode shape) exhibits a "hard" flutter mechanism at a margin of 0.89 (relative to the dive speed), whereas the third and fourth structural modes (an in-plane bending mode, and a torsional mode, respectively), exhibit softer hump modes, with margins of 0.76 and 1.04. Clearly the flutter constraints are violated by this wing structure, which is the goal of the next 2 design stages in Fig. 9. Constraint boundaries are set to margins of 1.0 for open-loop and 1.2 for closed-loop. As with the MLA load cases in Table 1, the optimizer is forced to account for cases that do not benefit from AFS (i.e., the open-loop constraint), albeit at a lower factor of safety: this prevents overly-large mass reductions, and injects a level of risk-reduction into the design process.

The second phase of Fig. 9 enforces the 1.0 open-loop flutter margin constraint only: structural mass increases from 13,870 to 14,358 kg, in order to satisfy this constraint. The third phase adds the 1.2 closed-loop flutter margin constraint to the design process, as well as the U_{LQR} design variable. During this design

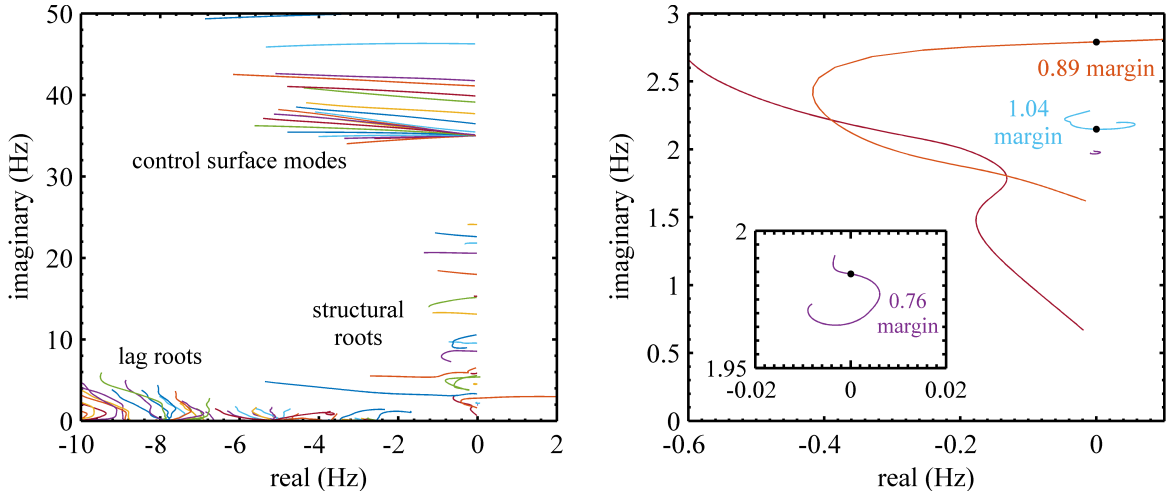

Figure 10. Eigenvalue migration behavior for the wing optimized without flutter constraints.

phase, the structural mass is essentially unchanged. The optimizer can meet this closed-loop constraint without needing to passively stiffen the wing, as the LQR controller is capable of stabilizing the system on its own. Eigenvalue migration of the open- and closed-loop dynamics for this case are shown in Fig. 11. The constraint boundaries computed with Eq. 10 are shown in the figure as well. Both constraint boundaries are highly-active, with two modes interacting with the constraint boundary in the open-loop case, and three modes in the closed-loop case.

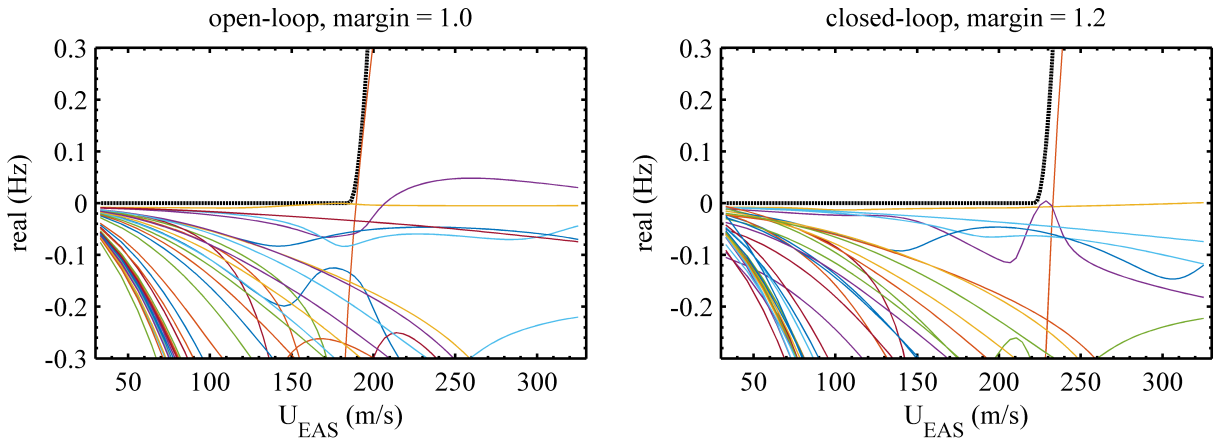

Figure 11. Open- and closed-loop eigenvalue migration (real part); constraint boundary indicated by thick dashed line.

The fourth and fifth phases of Fig. 9 add the control surface layout design variables (x_i, which impact the AFS problem through Eq. 7), and the δ_x constraint, respectively. Only during these final stages does the actuator mass change, dropping from 2,262 kg to 232 kg, retaining only three control surfaces near midspan (seen in Fig. 12). As with the previous MLA control surface layouts, the low effectiveness of the outboard control surfaces makes these actuators unattractive choices for AFS as well. Structural mass increases only slightly during this stage, from 14,358 to 14,377 kg. This suggests, as before, that the LQR controller is capable, even with only 3 control surfaces, of meeting the closed-loop flutter constraint without requiring any passive stiffening from the structural design variables.

The previous MLA results of Fig. 8 considered the change in optimal control surface layout when the number of actuators was gradually forced to zero. This would not be an interesting exercise here, given the simple AFS layout. It is of interest, however, to understand the role of a control cost constraint on J (Eq. 9). The bar heights in Fig. 12 indicate the contribution of each actuator to the $\boldsymbol{u}_{ASE}^T \cdot \boldsymbol{R} \cdot \boldsymbol{u}_{ASE}$ portion of Eq. 9 (the $\boldsymbol{x}_{ASE}^T \cdot \boldsymbol{Q} \cdot \boldsymbol{x}_{ASE}$ portion is not shown). Quantified control cost and design mass for each case in Fig. 12

is shown in Table 3. For the left two plots in Fig. 12, the case where all actuators are used for AFS has a J value of 41, whereas the case with only 3 actuators has a J value of 2,380. Clearly, the optimizer is able to remove most of the control surfaces and still satisfy the closed-loop flutter constraint, but only at the expense of having an excessive control cost-per-actuator. This can also be inferred from Fig. 13, which show open- and closed-loop flutter mode shapes for the "hard" flutter mechanism of the second bending mode. Control surface deflections for the optimal layout (three actuators) are far larger, relative to the wing vibration, than seen in the case where all 20 actuators are used for AFS.

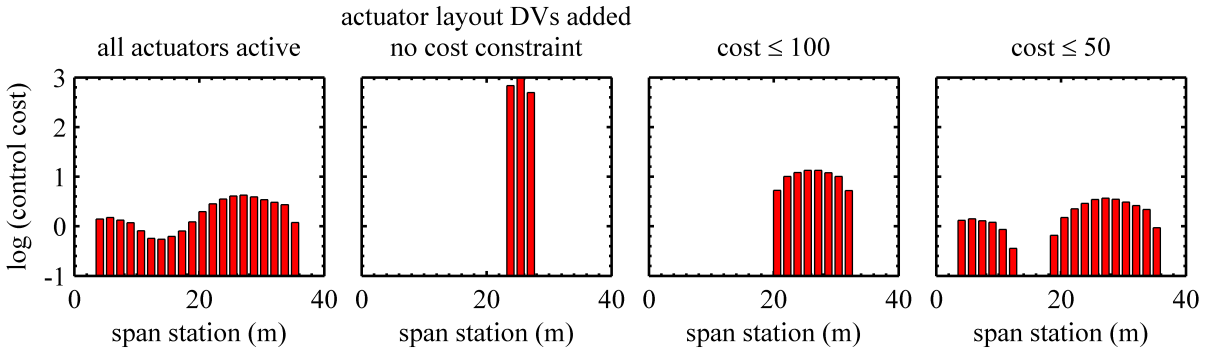

Figure 12. Actuator control cost distribution during AFS.

The remaining two designs in Fig. 12 and Table 3 enforce an upper bound on the control cost J, of 100 and 50, respectively. These constraints force the optimizer to use more actuators, with a lower cost-per-actuator. The design with a J constraint of 50 favors control surfaces at the root over using those near midspan. The reason for this is unclear, given that the control surfaces are not being used for static trim (as seen in the MLA results), but may be due to a disinclination to use control surfaces near the anti-node line of the flutter mode shape seen in Fig. 13.

Table 3. Summary of AFS designs corresponding to Fig. 12.

Number of Actuators	M	$M_{structure}$	$M_{actuator}$	Cost Constraint?	Cost
20	16,592 kg	14,358 kg	2,262 kg	no	41
3	14,610 kg	14,377 kg	232 kg	no	2,380
8	14,761 kg	14,176 kg	585 kg	yes	100
17	16,341 kg	14,479 kg	1,862 kg	yes	50

It can also be seen from Table 3 that, while both actuator mass and the summed actuator-structural mass (the objective function) monotonically increase as the cost constraint is made harder to satisfy, structural mass does not. Furthermore, the changes in structural mass are small. As noted above, a meaningful increase in structural mass would only occur in a situation where the LQR feedback control, designed by the optimizer, is unable to entirely meet the closed-loop control margin on its own. The optimizer would then be forced to utilize the structural design variables to stiffen the wing to help meet this constraint, which would make the wingbox heavier. For the current configuration, such a situation would likely only occur under a hard-to-satisfy control cost constraint on J, and an additional constraint limiting the total number of actuators (such as done in Fig. 8). Alternatively, increasing the value of $\boldsymbol{R}$ in Eq. 9, which would increase the role of control surface motion in J,[22] may also force the optimizer to passively stiffen the wing rather than increase the number of actuators, when faced with a constraint on control cost.

VI. Conclusions

This work has considered aeroservoelastic optimization of the CRM wingbox via structural sizing design variables, control surface actuation/scheduling design variables, and control surface layout/topology design variables. Key findings are as follows:

- In all cases studied, the SIMP-based penalty on intermediate x_i variables is largely successful, pushing each of these variables to the desired extremes of zero or one (i.e., each control surface is fully removed or fully retained) as the aeroelastic optimization process converges. This successfully allows for gradient-based optimization of these layout design variables alongside a large number of structural sizing variables.
- For MLA, the basic mechanism exploited by the optimizer is to reduce bending moment with outboard control surfaces, but use inboard control surfaces to help maintain longitudinal trim. When allowed to remove control surfaces during layout design, the optimizer retains only those which are most important to this overall trimming mechanism. Control surfaces at the extreme wingtip are removed despite their large moment arm; low effectiveness is observed here due to the torsional flexibility of the wing.
- There is a conflict between actuator/control surface mass and structural mass during MLA. Decreasing actuator mass (by removing control surfaces) will limit the ability of the actuators to alleviate maneuver loads, thus prompting the optimizer to stiffen the wing, and increase its mass. This trade-off is relatively mild until the optimizer is forced to use less than 3 control surfaces. This destroys the aforementioned inboard-outboard trim mechanism, and the optimizer must passively stiffen the wing to clear the maneuver load cases, prompting large increases in structural weight.
- During AFS, the LQR controller is fully capable of meeting closed-loop flutter constraints without requiring the optimizer to passively stiffen the wing (increasing structural weight). When allowed to remove control surfaces during layout design, the optimizer is similarly capable of removing most of the actuators without a structural weight penalty. The resulting control cost (performance index) is very high, however.
- Adding a control cost constraint to the optimal AFS layout forces the optimizer to add more control surfaces, in order to spatially-distribute the cost burden. It is speculated that shifting the $\boldsymbol{Q}$ and $\boldsymbol{R}$ definitions in the LQR setup (Eq. 9) toward a situation with greater penalties on input actuation, may force the optimizer to retain fewer control surfaces and passively stiffen the wing, in order to meet a hard-to-satisfy cost constraint.

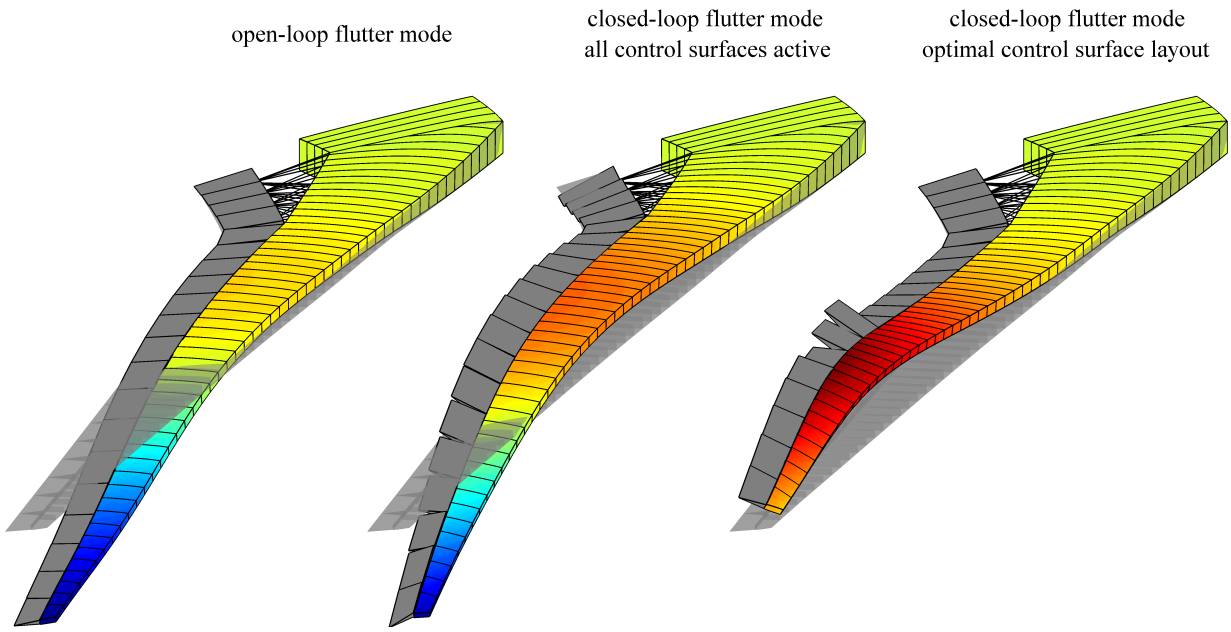

Figure 13. Open-loop flutter mode shape (left) and closed-loop flutter mode shapes for the design with a full bank of control surfaces (center), and the design with the optimal control surface layout (right).

Acknowledgments

This work is funded by the NASA Advanced Air Transport Technologies project.

References

[1]Zeiler, T., Weisshaar, T., "Integrated Aeroservoelastic Tailoring of Lifting Surfaces," *Journal of Aircraft*, Vol. 25, No. 1, pp. 76-83, 1988.

[2]Livne, E., Schmidt, L., Friedmann, P., "Integrated Structure/Control/Aerodynamic Synthesis of Actively Controlled Composite Wings," *Journal of Aircraft*, Vol. 30, pp. 387-394, 1993.

[3]Bindolino, G., Ricci, S., Mantegazza, P., "Integrated Servostructural Optimization in the Design of Aerospace Systems," *Journal of Aircraft*, Vol. 36, pp. 167-175, 1999.

[4]Zink, P., Mavris, D., Raveh, D., "Maneuver Trim Optimization Techniques for Active Aeroelastic Wings," *Journal of Aircraft*, Vol. 38, No. 6, pp. 1139-1146, 2001.

[5]Padula, S., Kinkaid, R., "Optimization Strategies for Sensor and Actuator Placement," NASA/TM-1999-209126.

[6]Nam, C., Kim, Y., "Optimal Design of Composite Lifting Surface for Flutter Suppression with Piezoelectric Actuators," *AIAA Journal*, Vol. 33, No. 10, pp. 1897-1904, 1995.

[7]Chattopadhyay, A., Seeley, C., Jha, R., "Aeroelastic Tailoring using Piezoelectric Actuation and Hybrid Optimization," *Smart Materials and Structures*, Vol. 8, pp. 83-91, 1999.

[8]Johnson, T., Athans, M., Skelton, G., "Optimal Control-Surface Locations for Flexible Aircraft," *IEEE Transactions on Automatic Control*, Vol. AC-16, No. 4, pp. 320-331, 1971.

[9]Weisshaar, T., Nam, C., "Aeroservoelastic Tailoring for Lateral Control Enhancement," *Journal of Guidance, Control, and Dynamics*, Vol. 13, No. 3, pp. 458-465, 1990.

[10]Viswamurthy, S., Ganguli, R., "Optimal Placement of Trailing-Edge Flaps for Helicopter Vibration Reduction using Response Surface Methods," *Engineering Optimization*, Vol. 39, No. 2, pp. 185-202, 2007.

[11]Kolonay, R., Kobayashi, M., "Optimization of Aircraft Lifting Surfaces using a Cellular Division Method," *Journal of Aircraft*, Vol. 52, No. 6, pp. 2051-2063, 2015.

[12]Bendsøe, M., Sigmund, O., *Topology Optimization - Theory, Methods, and Applications*, Springer, New York, 2003.

[13]Vassberg, J., DeHaan, M., Rivers, S., Wahls, R., "Development of a Common Research Model for Applied CFD Validation Studies," *AIAA Applied Aerodynamics Conference*, Honolulu, Hawaii, August 10-13, 2008.

[14]Kenway, G., Martins, J., Kennedy, G., "Aerostructural Optimization of the Common Research Model Configuration," *AIAA Aviation Conference*, Atlanta, GA, June 16-20, 2014.

[15]Stroud, W., Agranoff, N., "Minimum-Mass Design of Filamentary Composite Panels under Combined Loads: Design Procedure Based on Simplified Buckling Equations," NASA TN D-8257, 1976.

[16]Appa, K., "Finite-Surface Spline," *Journal of Aircraft*, Vol. 26, No. 5, pp. 495-496, 1989.

[17]Kreisselmeier, G., Steinhauser, R., "Systematic Control Design by Optimizing a Vector Performance Index", *International Federation of Active Controls Symposium on Computer-Aided Design of Control Systems*, Zurich, Switzerland, 1979.

[18]Svanberg, K., "A Class of Globally Convergent Optimization Methods Based on Conservative Convex Separable Approximations," *SIAM Journal of Optimization*, Vol. 12, pp. 555-573, 2002.

[19]Adelman, H., Haftka, R., "Sensitivity Analysis of Discrete Structural Systems," *AIAA Journal*, Vol. 24, No. 5, pp. 823-832, 1986.

[20]Roger, K., "Airplane Math Modeling Methods for Active Control Design," AGARD CP-228, pp. 4-11, 1977.

[21]Kline, K., "Dynamic Analysis Using a Reduced Basis of Exact Modes and Ritz Vectors," *AIAA Journal*, Vol. 24, No. 12, pp. 2022-2029, 1986.

[22]Stevens, B., Lewis, F., *Aircraft Control and Simulation*, John Wiley and Sons, Hoboken, NJ, 2003.

[23]Ringertz, U., "On Structural Optimization with Aeroelasticity Constraints," *Structural Optimization*, Vol. 8, pp. 16-23, 1994.

[24]Gilbert, M., "An Analytical Sensitivity Method for use in Integrated Aeroservoelastic Aircraft Design," *Mechanical Systems and Signal Processing*, Vol. 4, No. 3, pp. 215-231, 1990.